Enhancing the Power Output of Bifacial Solar Modules by Applying Effectively Transparent Contacts (ETCs) With Light Trapping

Rebecca Saive, Thomas C. R. Russell, and Harry A. Atwater

***Abstract*—We have performed a computational study on the enhancement of the power output of bifacial solar modules with effectively transparent contacts (ETCs). ETCs are triangular cross-sectional silver grid fingers that redirect light to the active area of the solar cell, therefore mitigating grid finger shading losses. Furthermore, ETCs can be spaced densely leading to light trapping. We modeled bifacial silicon heterojunction solar modules with varying front and rear illumination and ETC coverages. We determined that shading losses can be almost fully mitigated and that light absorption can be increased by up to 4.7% compared with state-of-the-art screen-printed bifacial modules. Furthermore, we calculated that grid resistance and silver usage can be improved when using ETCs.**

***Index Terms*—Bifacial solar modules, effectively transparent contacts (ETCs), light trapping.**

I. Introduction

BIFACIAL solar cells have been gaining momentum due to their promise for price reductions of photovoltaic (PV) generated electricity by increasing power output [1], [2]. In addition to front-side illumination, bifacial solar cells also accept photons incident on the rear side. Following initial introduction of the concept in the 1960s [3], studies have found surprisingly higher power output than for monofacial solar modules. An increase in power output of up to 50% has been reported [4]. A more recent study even reported an increase of 40%–70% under cloudy conditions and between 13% and 35% under sunny conditions, depending on the height of the ground clearance [5]. Other factors such as the spectral albedo of the surroundings [6]–[9] as well as the cell mounting geometry (see Fig. 1) strongly influence the power output [7], [10]–[16]. However, increased photon acceptance only translates into increased power output if charge carriers can be extracted and transported efficiently. Silicon solar cells, which presently dominate more than 90% of the PV market [17] are to date the only commercial bifacial technology [18], and for these cells the collected photocurrent is conducted to the busbar by screen-printed silver contacts. Due to the shading of these metal contacts, between 2% and 8% of the incident light is lost [19]. Several approaches for alternative contact designs have been reported that aim to decrease shading loss [20]–[24].

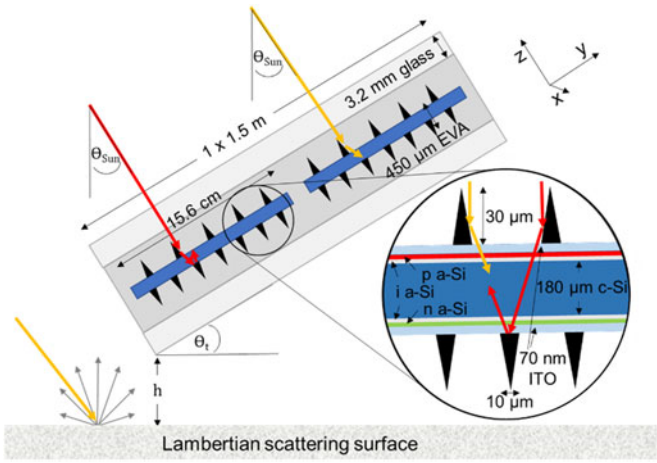

Fig. 1. Schematic of the cross section of a bifacial silicon heterojunction solar module with effectively transparent contacts.

We have recently developed effectively transparent contacts (ETCs), with record-high optical transparency that mitigate a large fraction of these shading losses without sacrificing the charge conduction [25]–[28]. Since interdigitated back contacts cannot be straightforwardly applied to bifacial solar modules, ETCs currently constitute the only solar cell contact technology that can achieve shading loss of less than 0.1% for bifacial solar cells. We have also recently shown that densely spaced ETCs can enhance light trapping in thin silicon solar cells [29], [30].

Here, we demonstrate computationally how ETCs can enhance absorption in bifacial silicon heterojunction cells and modules by efficiently redirecting light into the solar cell and by trapping light within the crystalline silicon. Fig. 1 shows schematically a bifacial solar module with ETCs on front and rear side of silicon heterojunction cells. The front side experiences mostly direct illumination from the sun, while the rear

Manuscript received April 5, 2018; revised May 31, 2018; accepted June 3, 2018. This work was supported in part by the Engineering Research Center Program of the National Science Foundation (NSF) and the Office of Energy Efficiency and Renewable Energy of the Department of Energy under NSF Cooperative Agreement EEC-1041895 and in part by the U.S. Department of Energy through the Bay Area Photovoltaic Consortium under Award DE-EE0004946. The work of R. Saive was supported by the Global Climate & Energy project. *(Corresponding author: Rebecca Saive.)*

The authors are with the Thomas J. Watson Laboratories of Applied Physics and Material Science, California Institute of Technology, Pasadena, CA 91125 USA (e-mail: r.saive@utwente.nl; thomruss@caltech.edu; haa@caltech.edu).

Color versions of one or more of the figures in this paper are available online at http://ieeexplore.ieee.org.

Digital Object Identifier 10.1109/JPHOTOV.2018.2844850

side is exposed to diffuse light reflected from the surroundings. With ETCs, photons incident on a metal contact are efficiently redirected to the active area due to the triangular geometry of ETCs (see Fig. 1, yellow arrow). Low-energy photons that are not absorbed during the first pass can be reflected back at the flat bottom of the ETCs, leading to light trapping (see Fig. 1, red arrow). We performed computational optical simulations of different front and rear illumination scenarios. Furthermore, we calculated the grid resistance of the investigated contact layouts. We found that using ETCs, the number of busbars can be reduced compared with a standard bifacial solar cell contact grid layout. This leads to a decrease in silver consumption as well as to an additional advantage for photon absorption.

II. Optical Modeling

As depicted in Fig. 1, we assume that a bifacial module accepts mostly direct irradiation at the front and mostly diffuse light at the rear. Under clear sky conditions, this is a realistic assumption, while under cloudy conditions there is also a significant diffuse light portion incident on the front side. We show below that the optimal grid configuration for front side direct or diffuse illumination is similar. At first, we consider the clear sky case. We assume that the total wavelength (λ) dependent irradiance ($I_{\text{total}}(\lambda)$) incident is given by the sum of front (I_{front}) and rear (I_{rear}) illumination

$$I_{\text{total}}(\lambda) = I_{\text{front}}(\lambda) + I_{\text{rear}}(\lambda). \tag{1}$$

On the front, we assume AM 1.5G (ASTM G-173-03) irradiation

$$I_{\text{front}}(\lambda) = \text{AM1.5G}(\lambda). \tag{2}$$

On the rear side, the irradiation depends on the initial solar irradiance (AM1.5G(λ)), on the wavelength (λ) dependent albedo $R_A(\lambda)$, on the angle of incidence and on geometric factors—which we summarize in a constant C ($0 \leq C \leq 1$). Here, we define the angle parallel to the grid fingers as the x-axis and the angle perpendicular to the grid fingers as the y-axis. The wavelength and angle-dependent rear illumination is given by the following:

$$I_{\text{rear}}(\lambda, x, y) = \text{AM1.5G}(\lambda) \cdot C \cdot R_A(\lambda) \cdot \cos(x, y). \tag{3}$$

The short-circuit current density generated by a photon with wavelength λ ($j(\lambda)$) can be determined if the external quantum efficiency (EQE(λ)) is known and the internal quantum efficiency is assumed to be one. For the front, we obtain the following expression:

$$j_{\text{front}}(\lambda) = \text{EQE}_{\text{front}}(\lambda) \cdot \text{AM1.5G}(\lambda). \tag{4}$$

For the rear side, we obtain the following expression:

$$j_{\text{rear}}(\lambda, x, y) = \text{EQE}_{\text{rear}}(\lambda, x, y) \cdot \text{AM1.5G}(\lambda) \cdot C \cdot R_A(\lambda) \cdot \cos(x, y). \tag{5}$$

By weighting and averaging $\text{EQE}_{\text{rear}}(\lambda, x, y)$ with the $\cos(x, y)$, we obtain an angle-independent EQE ($\text{EQE}_{\text{rear}}(\lambda)$) that contains the cosine intensity distribution of the diffuse light

$$\text{EQE}_{\text{rear}}(\lambda) = \frac{1}{2\sum_{x=0}^{90}\cos(x)} \times \left(\sum_{x=0}^{90}\text{EQE}(\lambda, x)\cos(x) + \sum_{y=0}^{90}\text{EQE}(\lambda, y)\cos(y)\right). \tag{6}$$

Therefore, we obtain as expression for the total short-circuit current density (j_{total})

$$j_{\text{total}} = \int_{\lambda_{\min}}^{\lambda_{\max}} (\text{AM1.5G}(\lambda) \cdot \text{EQE}_{\text{front}}(\lambda) + \text{AM1.5G}(\lambda) \cdot C \cdot R_A(\lambda) \cdot \text{EQE}_{\text{rear}}(\lambda)) \cdot d\lambda. \tag{7}$$

We performed optical simulations in order to determine the EQE of bifacial silicon heterojunction solar modules for front- and rear-side illumination. We chose a thickness of 180 μm for the monocrystalline silicon absorber, which is passivated by a 5 nm layer of intrinsic amorphous silicon. Front and rear of the crystalline silicon exhibit random texture (not shown in Fig. 1). The front-side selective contact is a 5-nm p-doped amorphous silicon layer and the rear-side selective contact is 5-nm n-doped amorphous silicon. The front and rear both have a 70-nm indium tin oxide (ITO) layer in order to achieve good lateral charge transport and antireflection properties. We found $\sim$70 nm is the required thickness of ITO to provide optimal antireflection properties in multiple spectral albedo scenarios [31]. On front and rear, we assumed an encapsulation consisting of 450-μm EVA [32] and 3.2 mm glass [33] with antireflection coating [34]. We performed simulations of modules without any metal contacts in order to have a reference for determining shading losses and light trapping. As reference for a state-of-the-art optimal screen-printed contact, we used the shape and shading of double screen-printed contact fingers [35]. These contact fingers are $\sim$17 μm high and $\sim$46 μm wide, and feature rounded shapes [35]. The metal coverage of reference contact fingers was assumed to be 3.4% at the front and 4.8% at the rear [19]. Three busbars with a total coverage of 2.4% were used for front and rear sides, which are 1.25 mm wide and 200 μm high [19]. ETC grids were simulated assuming no, one, two, or three busbars with the same properties as those for the reference case. ETCs were composed of triangular cross-sectional silver lines (complex refractive index obtained from [36]) with 10 μm width and 30 μm height. Comparison of simulations with experimental results presented in [25]–[27] show that using specular side walls with the optical properties of bulk silver [36] is in good agreement with the experiment. In the experiments, specular side walls were obtained via performing an imprint process with a silver nanoparticle ink [25]–[27], [37]. The performance dependence on shape and dimension of the metal contact was investigated elsewhere [30] and it was determined that a width of greater than 2.5 μm has to be used in order to avoid resonant interaction with light. Furthermore, the lateral conductivity also increases with the increasing cross section. On the other hand, the performance decreases if the structures become too

large [30] due to large contiguous areas being shaded. From a practical perspective, on one hand, it is favorable to use a size that is significantly larger than the random pyramid texture of the silicon, on the other hand, it should not be too large in order not to interfere with standard processing procedures. The largest structures we processed in our laboratory were 10 μm wide and 30 μm high.

The module size was assumed to be a single cell standard module with the dimension 15.6 cm $\times$ 15.6 cm. The front and rear coverage was varied between 5% and 50% to obtain the optimal configuration.

In order to obtain an accurate representation of the thin-film optical properties of the solar cell while also simulating micro and millimeter scale features with computational fidelity, we used a two-step simulation method. First, we simulated the reflection, transmission, and parasitic absorption at the interface between EVA and the solar cell via thin-film simulations performed with PV Lighthouse's OPAL 2 [38]. This solver calculates the propagation of light through thin films using the transfer matrix method. The optical properties at the interface were obtained for angles of incidence between 0° and 89° to the surface normal for the cases of front and rear illumination. N-doped amorphous silicon exhibits higher parasitic absorption than p-doped amorphous silicon, therefore, front and rear were simulated individually. These transmission and reflection data were passed to a Synopsis LightTools ray optical simulation model. In this model, the optical elements, their surface, and bulk properties are defined. The LightTools software uses Monte Carlo ray tracing in order to simulate the propagation of light from a defined source to a receiver. Only ray optical behavior of light can be treated, hence we included the PV Lighthouse OPAL 2 thin-film results as surface properties in the model. We verified our simulations by comparison with OPAL 2 combined thin film and Monte Carlo ray tracing as well as with rigorous coupled wave analysis. The full module consists of a 180 μm absorber with the bulk optical properties of crystalline silicon [39], while the surface on front and back side is defined by the OPAL 2 results. The EVA and glass are explicitly included in the LightTools model, and so are busbars, screen-printed fingers, and ETCs. Note that with this approach we also ensured accurate accounting for total internal reflection at the glass/air interface [40]. In all cases, we simulated the total reflection and the absorption in every single layer. In particular, we obtained the absorption within the crystalline silicon and accounted for parasitic absorption within the other layers. In the following sections, we will investigate front and rear illumination separately, and we present the overall result in Section V.

III. Front-Side Illumination

We investigated the effect of different contact layouts on the absorption within the crystalline silicon, assuming illumination only from the front side. Fig. 2 shows the corresponding spectral EQE for a module with the reference double screen printed fingers (schematic A, black solid curve), for a module without any metallization (schematic B, black dashed curve), and for a module with 20% ETC coverage on the front and 50% ETC coverage on the rear (schematic C, red curve). These three curves

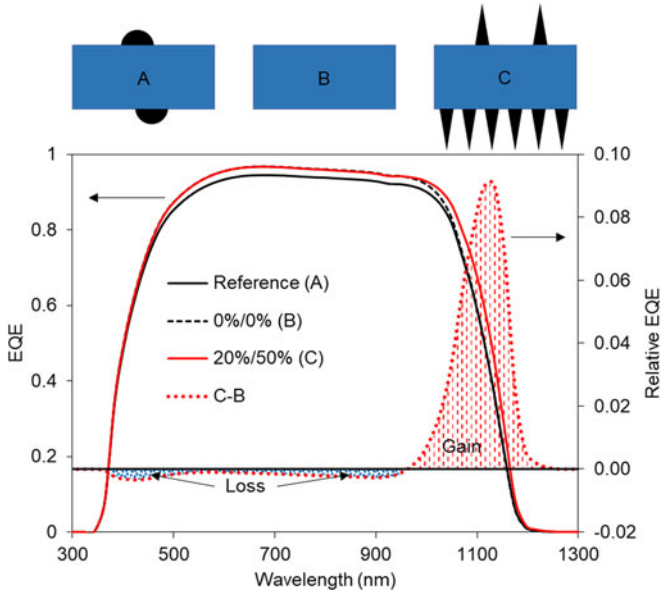

Fig. 2. (Left ordinate) Simulated EQE of a bifacial cell with front-side illumination and no metallization (black dashed curve), double screen-printed reference fingers (black curve) and ETCs with 5% coverage on the front and 50% on the rear side (red curve). (Right ordinate) Relative EQE displayed as subtraction of the EQE with ETCs and without metallization (dashed red curve).

refer to the left ordinate. In all cases, shading from busbars was neglected. The reference fingers lower the EQE, while ETCs perform similarly to a module without metallization for wavelengths shorter than 1000 nm. For longer wavelengths, the EQE with ETCs even exceeds the EQE of a module without metallization. This effect results from light trapping. Light that was not absorbed in the first path has a probability (dependent on the rear ETC coverage) to be reflected at the flat bottom of the rear ETCs. In order to make the difference between ETCs and no metallization clearly visible, we subtracted the EQE with ETCs by the EQE without ETCs. The result is shown as the red dashed curve in Fig. 2 and refers to the right ordinate. The loss compared with no contacts is shown by the blue shaded area, and the gain is shown by the red shaded area. It can be seen that ETCs yield a slightly lower EQE in the shorter wavelength regime than no metallization. For short wavelengths, this result is mostly due to parasitic absorption within the silver of the ETCs. Furthermore, due to a change in the angle of incidence after redirection by the ETCs, the antireflection properties become slightly worse, which leads to an additional loss. However, the EQE is significantly increased in the longer wavelength regime due to light trapping, which exceeds the losses in the shorter wavelength regime. We investigated multiple front and rear ETC coverage scenarios, the results of which are presented in Fig. 3. The EQE was weighted with the AM 1.5G spectrum to obtain the short-circuit current density (j_{front}) as shown in (7). All configurations were compared with the case without any metallization, and the percentage change of j_{front} in each, relative to this case, is depicted. Negative values mean losses due to shading, while positive values can be attributed to light trapping. We can see that the reference with screen-printed fingers loses 2.3% j_{front} from shading. For the ETCs, losses increase for the increased

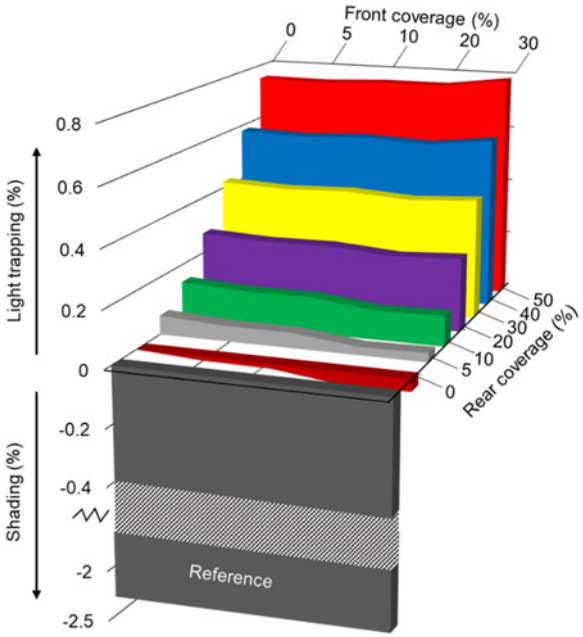

Fig. 3. Light trapping and shading loss (without busbars) of the reference grid and ETCs with different front and rear coverage displayed as the change in AM 1.5G weighted absorption compared with a bifacial module without metallization.

front coverage if the rear is not covered with metal. However, the losses never exceed 0.1%, which corresponds to an effective transparency >99.9%. But with increased rear-side coverage, the light trapping increases and j_{front} exceeds the no metallization case by up to 0.79%. It can be seen that for increased rear coverage, increased front coverage contributes stronger to the light trapping as well. With increased rear coverage the chances increase that long wavelength photons undergo a second pass, as depicted by the red arrow in Fig. 1. Only photons that are first reflected at the rear can experience light trapping from the front-side ETC coverage.

Therefore, the light trapping on the front increases with the increased rear light trapping. Busbar losses are neglected in Fig. 3 in order to focus on the finger and ETC properties. Each added busbar contributes another 0.8% shading loss. In our reference cell with three busbars, this adds up to 2.4% additional shading. We will demonstrate below that with ETCs we can reduce the number of busbars down to one, leading to additional gain in effective transparency.

IV. Rear-Side Illumination

We compared the optical performance of the reference finger grid and ETCs when exposed to rear-side illumination. We assume Lambertian light scattering of sunlight from the surroundings and therefore, randomized light incident on the rear. As light is incident from all angles, first we need to determine the angle-dependent EQE for all different front- and rear-side coverages. We performed the same optical simulation as described above but varied the angle of incidence between 0° and 80° to the surface normal. The angle was varied along the *x*-axis, which is parallel to the finger grid lines, and along the *y*-axis, which is perpendicular to the finger grid lines. As described in Section II and in (6), the angle-dependent EQE needs to be weighted with a cosine factor. Fig. 4 shows the angle-dependent rear-side short-circuit current density (j_{rear}) calculated using (5)–(7), for the reference double screen-printed metallization, and for ETCs with 20% coverage on the front and varying coverage on the rear. The left side of the graph shows j_{rear} for light incident along the *y*-axis and the right side shows j_{rear} for light incident along the *x*-axis. Normal incidence (0°) is in the center. Note that the light is incident from the rear and the rear coverage is changed between 0% and 50%, while the front coverage is kept constant. Furthermore, the rear uses n-doped amorphous silicon, and therefore light incident on the rear experiences slightly higher parasitic absorption within the amorphous layer than light incident on the front. For 0°, we obtain a similar result as in Fig. 3: ETC grids perform optically similar to no metallization, while the reference grid exhibits 2.9% loss. The higher loss compared with the front results from the higher metal coverage on the rear for the reference we used [19]. With increasing angle along the *x*-axis, the current density decreases for all contact layouts due to a decrease in EQE and due to the cosine factor. The EQE decreases with the increasing angle of incidence due to a less favorable behavior of the antireflection coating. Along the *x*-axis, ETCs always outperform the reference case and the ETC coverage has no influence. For light incident from the *y*-axis, the current density depends on the ETC coverage. For steep angles, there is no dependence but for increasing angle the current density experiences a cutoff for high ETC coverage. For high coverage and high incident angle, ETCs shade the active area and light incident on the metal lines is likely to be reflected to a neighboring metal line instead of the active area. Therefore, the cutoff angle decreases with the increasing coverage. For 20% coverage, the current density always stays above the reference case, for 30% coverage it crosses the reference case at 50°, for 40% coverage at 40°, and for 50% coverage at 30°.

V. Optimal Front and Rear Configuration

In Sections III and IV, we have shown the effects of different ETC front and rear coverage for both front and rear illumination separately. For front illumination, higher rear coverage leads to increased EQE due to light trapping. Meanwhile, as Fig. 4 shows, increased rear coverage leads to a cutoff in current generation for light that is incident under an oblique angle parallel to the *y*-axis. Our goal is to obtain the highest current generation overall, i.e., to maximize the sum of the currents generated from front and rear illumination. We use the equation introduced in Section II to derive the optimal configuration assuming mostly direct illumination under normal incidence from the front and diffuse light from the rear side. First, we calculate j_{total} according to (7) by using the EQE results obtained in Sections III and IV. For our calculation, we assume a spectrally independent albedo ($R_A(\lambda) = \text{constant}$) and incorporate it into the constant C. In this case, front-side and rear-side illumination experience the same wavelength dependence. Therefore, the rear-side illumination can be expressed as a fraction of the front-side illumination, this fraction being dependent on the

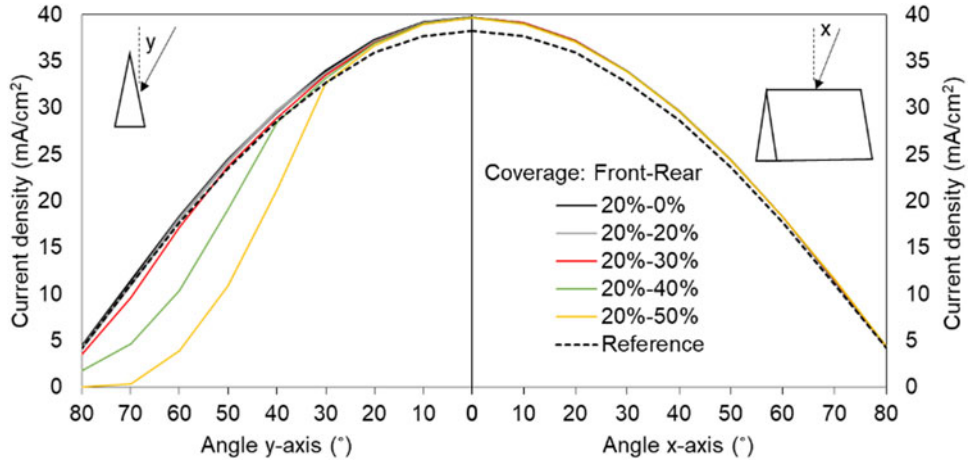

Fig. 4. Generated current density for rear-side illumination depending on the ETC rear coverage and on the angle of incidence, assuming ETC front coverage of 20%. The left side is for light incident along the *y*-axis, the right side for light incident along the *x*-axis. The center presents normal incidence. This result is already multiplied with a cosine factor to account for lower intensity of light incident under an angle.

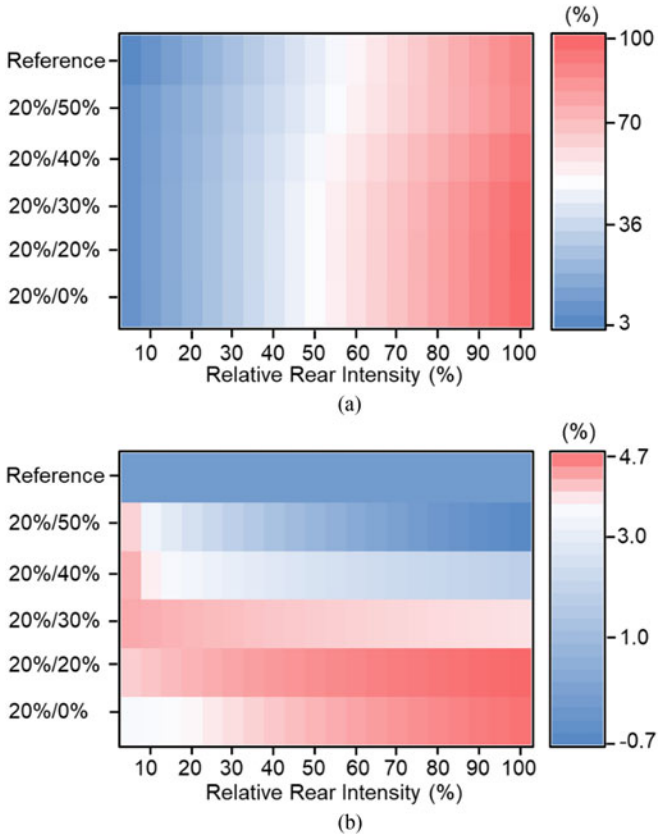

Fig. 5. Current density depending on the rear illumination intensity for different contact configuration. (a) Compared with reference monofacial module. (b) Compared with reference bifacial module.

albedo and the geometric factors. First, we calculate the total current density j_{total} and compare the result with the case of a monofacial solar module with the reference screen-printed contact fingers. Furthermore, as we will see in Section VI, we can reduce the number of busbars down to one if we use a front ETC coverage of more than 14%. Fig. 5(a) shows the relative current density for different rear intensities and different contact configurations compared with a monofacial cell with the reference screen-printed contacts. It can be seen that the bifacial reference current exceeds the monofacial current for all cases, although the module does not have a rear reflector, and therefore exhibits lower light trapping. This nicely demonstrates why bifacial solar modules generate more power whenever there is any possibility for light incident on the rear. In addition, the current density is increased even further when replacing the reference contact grid by ETCs. In order to investigate this effect more closely, we calculated the relative change in current density when using ETCs compared with the reference bifacial module. The results are presented in Fig. 5(b). The results from the reference are included, indicating the constant reference current density (0% change). In almost all cases, ETCs exceed the reference. Only for 50% rear coverage, the current cutoff for light incident from the *y*-axis dominates and the overall current density is decreased. The lower the rear illumination intensity, the more beneficial it is to use a higher ETC coverage on the rear. For less than 15% relative rear illumination intensity, an optimum coverage is achieved at 30% rear coverage and yields a relative current density increase of 4.4%. For a rear illumination intensity greater than 15%, a rear coverage of 20% offers optimal conditions and leads to a current density increase of 4.5%–4.7% depending on the rear illumination intensity. Note that this result takes into account that the ETCs use two fewer busbars, which correspond to a shading advantage of 1.6%.

VI. Metal Grid Conductivity and Silver Usage

In order to benefit from the increase in photon absorption by the use of ETCs, the grid resistance must not increase. Therefore, we calculated the grid resistance [41] of the reference with standard fingers and three busbars as well as that of ETCs with different coverage and one, two, or three busbars. The results are presented in Fig. 6(a). We assumed an ink with conductivity of 4.5 $\mu\Omega$-cm [42] and multiple busbar-ribbon connection pads. Use of a different ink would change the absolute series resistance values of the grids but would not alter the comparison between ETCs and the reference we use, as the series resistance

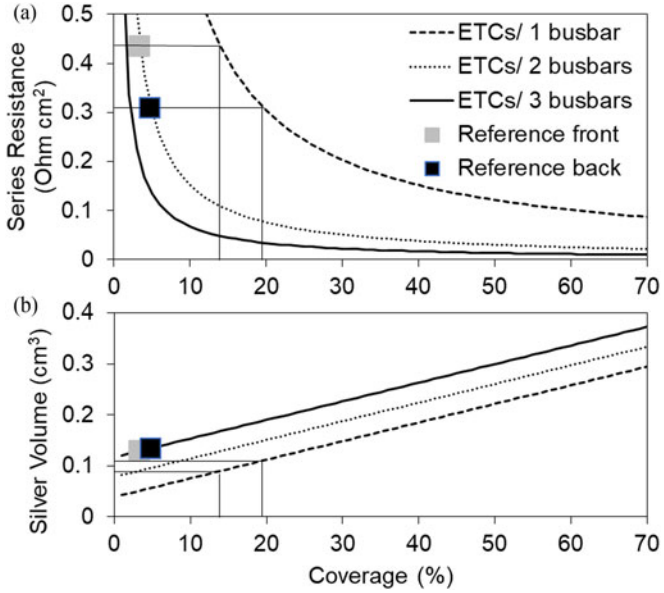

Fig. 6. (a) Series resistance and (b) silver consumption of the reference grid and ETC grids with different coverages and one, two, or three busbars.

scales linearly with the ink conductivity [41]. We obtained a grid resistance of 4.4 Ω-cm^2 for the reference front-side grid and 3.1 Ω-cm^2 for the rear-side grid. In Fig. 6(a), the series resistance results are presented for the reference (for front and rear grid) and for ETCs with one, two, or three busbars and different ETC coverages. It can be seen that if an ETC coverage of $>14\%$ is used on the front, only one busbar is necessary in order to achieve lower series resistance than for the reference. The respective coverage for the rear side amounts to $>20\%$.

If two busbars can be removed compared with the reference, another additional 1.6% j_{sc} increase is obtained compared with the cases presented in Fig. 3. In Section V, it was determined that the optimal front coverage is 20% and the optimal rear coverage is 20%–30%. In both cases, we assumed one busbar. From the results in Fig. 6(a), we can see that this is a configuration that leads to lower series resistance than for the reference.

Finally, we analyze the silver ink usage for the different grid configurations considered. The results are summarized in Fig. 6(b). The front and rear reference grid results are shown as grey and black squares, respectively. The silver usage for grids with different ETC coverage is shown in black solid (three busbars), black dotted (two busbars), and black dashed curves (one busbar). It can be seen that with one busbar, the ETCs do not exceed the silver usage of the reference as long as the coverage is below 25%. Therefore, the bifacial grid configurations considered above give rise to superior performance as compared with the state-of-the-art bifacial metallization in terms of optical transparency, series resistance, and ink consumption.

VII. Conclusion

We have shown that replacing screen-printed contact fingers by ETCs can lead to a significant enhancement in light absorption for bifacial solar modules. The microscale triangular cross-sectional ETCs redirect incoming light efficiently to the active area of the solar cell, mitigating shading losses. Their close spacing leads to light trapping for long wavelength photons, yielding an additional increase in light absorption. The close spacing also allows the use of one instead of three busbars, further decreasing shading as well as the amount of silver used. Our analysis suggests an optimal grid layout consists of one busbar and 20% ETC coverage on the front and one busbar and 20%–30% ETC coverage on the rear. With this configuration, the total light absorption from front and rear can be increased by 4.4%–4.7% depending on the relative rear intensity. At the same time, the series resistance of the contact grid can be maintained or even reduced and the ink usage can be reduced by 15%. As an additional benefit, ETCs are compatible with the SmartWire busbar technology [43], an approach to decreasing the optical losses of busbars that is becoming increasingly utilized in industrial solar cells.

Acknowledgment

The authors would like to thank J. Lloyd for helpful advice on LightTools optical simulations and P. Jahelka for helpful discussion.

References

[1] R. Kopecek *et al.*, "Bifaciality: One small step for technology, one giant leap for kWh cost reduction," *Photovolt. Int.*, vol. 26, pp. 32–45, 2014.
[2] F. Fertig *et al.*, "Economic feasibility of bifacial silicon solar cells," *Prog. Photovolt., Res. Appl.*, vol. 24, pp. 800–817, 2016.
[3] M. Hiroshi, "Radiation energy transducing device," US3278811A, 1966.
[4] A. Cuevas, A. Luque, J. Eguren, and J. Del Alamo, "50 Per cent more output power from an albedo-collecting flat panel using bifacial solar cells," *Sol. Energy*, vol. 29, no. 5, pp. 419–420, 1982.
[5] C. E. Valdivia *et al.*, "Bifacial photovoltaic module energy yield calculation and analysis," in *Proc. IEEE Photovolt. Spec. Conf.*, 2017.
[6] T. C. Russell, R. Saive, A. Augusto, S. G. Bowden, and H. A. Atwater, "The influence of spectral albedo on bifacial solar cells: A theoretical and experimental study," *IEEE J. Photovolt.*, vol. 7, no. 6, pp. 1611–1618, Nov. 2017.
[7] A. Krenzinger and E. Lorenzo, "Estimation of radiation incident on bifacial albedo-collecting panels," *Int. J. Sol. Energy*, vol. 4, no. 5, pp. 297–319, 1986.
[8] M. Brennan, A. Abramase, R. W. Andrews, and J. M. Pearce, "Effects of spectral albedo on solar photovoltaic devices," *Sol. Energy Mater. Sol. Cells*, vol. 124, pp. 111–116, 2014.
[9] R. W. Andrews and J. M. Pearce, "The effect of spectral albedo on amorphous silicon and crystalline silicon solar photovoltaic device performance," *Sol. Energy*, vol. 91, pp. 233–241, 2013.
[10] L. Kreinin, A. Karsenty, D. Grobgeld, and N. Eisenberg, "PV systems based on bifacial modules: Performance simulation vs. design factors," in *Proc. IEEE 43rd Photovolt. Spec. Conf.*, 2016, pp. 2688–2691.
[11] C. Deline *et al.*, "Evaluation and field assessment of bifacial photovoltaic module power rating methodologies," in *Proc. IEEE 43rd Photovolt. Spec. Conf.* , 2016, pp. 3698–3703.
[12] C. W. Hansen *et al.*, "Analysis of irradiance models for bifacial PV modules," in *Proc. IEEE 43rd Photovolt. Spec. Conf.*, 2016, pp. 0138–0143.
[13] U. A. Yusufoglu *et al.*, "Analysis of the annual performance of bifacial modules and optimization methods," *IEEE J. Photovolt.*, vol. 5, no. 1, pp. 320–328, Jan. 2015.
[14] C. K. Lo, Y. S. Lim, and F. A. Rahman, "New integrated simulation tool for the optimum design of bifacial solar panel with reflectors on a specific site," *Renewable Energy*, vol. 81, pp. 293–307, 2015.
[15] B. Soria, E. Gerritsen, P. Lefillastre, and J. E. Broquin, "A study of the annual performance of bifacial photovoltaic modules in the case of vertical facade integration," *Energy Sci. Eng.*, vol. 4, no. 1, pp. 52–68, 2016.
[16] S. Guo, T. M. Walsh, and M. Peters, "Vertically mounted bifacial photovoltaic modules: A global analysis," *Energy*, vol. 61, pp. 447–454, 2013.
[17] F. Ise, "Photovoltaics report," *Fraunhofer ISE*, Freiburg, Germany, 2014.

[18] F. Fertig *et al.*, "Bifacial potential of single-and double-sided collecting silicon solar cells," *Prog. Photovolt., Res. Appl.*, vol. 24, pp. 818–829, 2016.
[19] E. Lohmüller *et al.*, "The HIP-MWT+ solar cell concept on n-type silicon and metallization-induced voltage losses," in *Proc. 29th Eur. Photovolt. Sol. Energy Conf. Exhib.*, 2014, pp. 635–641.
[20] J. van de Groep, P. Spinelli, and A. Polman, "Transparent conducting silver nanowire networks," *Nano Lett.*, vol. 12, no. 6, pp. 3138–3144, 2012.
[21] P. G. Kik, "Catoptric electrodes: transparent metal electrodes using shaped surfaces," *Opt. Lett.*, vol. 39, no. 17, pp. 5114–5117, 2014.
[22] V. K. Narasimhan, T. M. Hymel, R. A. Lai, and Y. Cui, "Hybrid metal–semiconductor nanostructure for ultrahigh optical absorption and low electrical resistance at optoelectronic interfaces," *ACS Nano*, vol. 9, no. 11, pp. 10590–10597, 2015.
[23] P.-C. Hsu *et al.*, "Performance enhancement of metal nanowire transparent conducting electrodes by mesoscale metal wires," *Nature Commun.*, vol. 4, 2013, Art. no. 2522.
[24] F. Afshinmanesh, A. G. Curto, K. M. Milaninia, N. F. van Hulst, and M. L. Brongersma, "Transparent metallic fractal electrodes for semiconductor devices," *Nano Lett.*, vol. 14, no. 9, pp. 5068–5074, 2014.
[25] R. Saive *et al.*, "Effectively transparent contacts (ETCs) for solar cells," in *Proc. IEEE 43rd Photovolt. Spec. Conf.*, 2016, pp. 3612–3615.
[26] R. Saive *et al.*, "Effectively transparent front contacts for optoelectronic devices," *Adv. Opt. Mater.*, vol. 4, no. 10, pp. 1470–1474, 2016.
[27] R. Saive *et al.*, "Silicon heterojunction solar cells with effectively transparent front contacts," *Sustain. Energy Fuels*, vol. 1, pp. 593–598, 2017.
[28] H. A. Atwater *et al.*, "Solar cells and methods of manufacturing solar cells incorporating effectively transparent 3D contacts," US15144807, 2016.
[29] R. Saive, A. Augusto, S. Bowden, and H. A. Atwater, "Enhanced light trapping in thin silicon solar cells using effectively transparent contacts (ETCs)," in *Proc. IEEE 44th Photovolt. Spec. Conf.*, 2017.
[30] R. Saive and H. A. Atwater, "Mesoscale trumps nanoscale: Metallic mesoscale contact morphology for improved light trapping, optical absorption and grid conductance in silicon solar cells," *Opt. Express*, vol. 26, no. 6, pp. A275–A282, 2018.
[31] T. Russell, R. Saive, and H. A. Atwater, "Thermodynamic efficiency limit of bifacial solar cells for various spectral albedos," in *Proc. IEEE 44th Photovolt. Spec. Conf.*, 2017.
[32] M. R. Vogt *et al.*, "Optical constants of UV transparent EVA and the impact on the PV module output power under realistic irradiation," *Energy Procedia*, vol. 92, pp. 523–530, 2016.
[33] M. R. Vogt *et al.*, "Measurement of the optical constants of soda-lime glasses in dependence of iron content and modeling of iron-related power losses in crystalline si solar cell modules," *IEEE J. Photovolt.*, vol. 6, no. 1, pp. 111–118, Jan. 2016.
[34] M. R. Vogt, "Development of physical models for the simulation of optical properties of solar cell modules," Ph.D. thesis, Technische Informationsbibliothek, Hanover, Germany, 2016.
[35] J. Lossen *et al.*, "Double printing nPERT cells with narrow contact layers," *Energy Procedia*, vol. 92, pp. 939–948, 2016.
[36] E. D. Palik, *Handbook of Optical Constants of Solids*. New York, NY, USA: Academic, 1998.
[37] R. Saive, C. R. Bukowsky, and H. Atwater, "Three-dimensional nanoimprint lithography using two-photon lithography master samples," arXiv:1702.04012v1, 2017.
[38] K. R. McIntosh and S. C. Baker-Finch, "OPAL 2: Rapid optical simulation of silicon solar cells," in *Proc. 38th IEEE Photovolt. Spec. Conf.*, 2012, pp. 000265–000271.
[39] M. A. Green, "Self-consistent optical parameters of intrinsic silicon at 300K including temperature coefficients," *Sol. Energy Mater. Sol. Cells*, vol. 92, no. 11, pp. 1305–1310, 2008.
[40] A. Blakers, "Shading losses of solar-cell metal grids," *J. Appl. Phys.*, vol. 71, no. 10, pp. 5237–5241, 1992.
[41] Sep. 2015. [Online]. Available: http://pveducation.org/pvcdrom
[42] P. Papet *et al.*, "19% Efficiency module based on Roth&Rau heterojunction solar cells and DAY4TM energy module concept", in *Proc. 26th Eur. Photovolt. Sol. Energy Conf. Exhib.*, 2011, pp. 3336–3339.
[43] T. Söderström, P. Papet, and J. Ufheil, "Smart wire connection technology," in *Proc. 28th Eur. Photovolt. Sol. Energy Conf.*, 2013, pp. 495–499.

Authors' photographs and biographies not available at the time of publication.